Astronomy
&
Astrophysics

VLA and Effelsberg observations of the interstellar medium around the runaway star WR 124

S. Cichowolski[1,2], S. Pineault[2], E. M. Arnal[3,4], and C. E. Cappa[3,4]

[1] Instituto de Astronomía y Física del Espacio (IAFE), CC67, Suc.28, 1428 Buenos Aires, Argentina
e-mail: scicho@iafe.uba.ar
[2] Département de Physique and Observatoire du Mont Mégantic, Université Laval, Ste-Foy, Québec, G1K 7P4, Canada
[3] Instituto Argentino de Radioastronomía, C.C.5, 1894 Villa Elisa, Argentina
[4] Facultad de Ciencias Astronómicas y Geofísicas, Universidad Nacional de La Plata, 1900 La Plata, Argentina

ABSTRACT

Aims. We present very large array (VLA) and Effelsberg radio continuum and 21 cm H I line observations of the interstellar medium (ISM) surrounding the runaway star WR 124 and the nebula M 1-67. The H I data have been used to investigate the effects that a star with a strong stellar wind and a high peculiar velocity has on the ISM.
Methods. The VLA 21 cm H I observations were combined with single-dish Effelsberg observations to produce a series of H I images sensitive to all angular scales from the VLA resolution limit (~46″) up to the primary field of individual VLA antennae (*FWHM* = 36′). MSX and IRIS images were used to analyze the infrared emission around the star. Because the star is highly supersonic with respect to its local ISM, the observed H I distribution around the star is interpreted in terms of a simple bow shock model.
Results. The analysis of the H I data reveals the presence of a cavity centered on the star at an LSR velocity of ~60 km s^{-1}, consistent with a distance estimate of 5 kpc for WR 124. A second H I cavity is observed located 10′ to the north of the stellar position, consistent with the direction of motion of WR 124. The VLA continuum image at 8.5 GHz shows a remarkable resemblance to the optical images. All available radio continuum data suggest a purely thermal spectrum for the nebula. The MSX and IRIS infrared data show a changing morphology with wavelength. The dust temperature deduced from the infrared luminosities is in agreement with previous observations of bow shocks.

Key words. ISM: bubbles – ISM: individual objects: WR 124 – stars: Wolf-Rayet – ISM: H II regions

1. Introduction

Massive stars have a prominent impact on their surrounding interstellar medium (ISM), as testified by observations of H II regions, stellar wind bubbles, and supernova remnants. Analyzing and modeling the interaction of massive stars with the ambient gas provides a wealth of information on aspects such as the physical processes at work in the interstellar gas and dust, the energetic output of massive stars in the form of ionizing radiation and stellar winds, and the large-scale dynamics of the ISM.

In this paper we analyze the ISM around the runaway star WR 124 (≡209 BAC), classified as a Population I WN 8 star (van der Hucht 2001). The nebula M 1-67 was discovered around the star by Minkowski (1946) during an Hα objective prism survey. He suggested that M 1-67 might be a planetary nebula since the Hα velocity is comparable to that of WR 124. The nebula was later classified as an H II region by Sharpless (Sh2-80, Sharpless 1959). However, the presence of a WR star and the observed N-enhancement and O-deficiency (Esteban et al. 1991) are typical of material ejected in a previous evolutionary phase. These findings point to a progenitor more massive than those usually associated with central stars of planetary nebula. Consequently M 1-67 was then classified as a WR ring nebula by these authors.

Crawford & Barlow (1991) also argued against a planetary nebula interpretation. If M 1-67 were a planetary nebula, the distance should be in the range 0.5 to 1.0 kpc (van der Hucht et al. 1985; Bertola 1964). However, Crawford & Barlow (1991)

showed that the distance of M 1-67 must lie in the range 4–5 kpc. Thus M 1-67 is likely a WR ring nebula.

Grosdidier et al. (1998) obtained an HST WFPC2 deep Hα image of M1-67 and noted that the nebulosity was very clumpy and did not show an overall global shell structure. The velocity structure of the nebula was investigated in complementary Fabry-Perot Hα observations (Grosdidier et al. 2001) obtained at the Canada-France-Hawaii Telescope. These authors concluded that a simple thick shell by itself could not explain the observed multiple radial velocities along the line of sight (LOS). Van der Sluys & Lamers (2003) carried out various numerical simulations and showed that the observational data of Grosdidier et al. (1998, 2001) were better interpreted in terms of a bow shock model. Using a fully analytic model describing the wind bow shock developed by Wilkin (1996), Van der Sluys & Lamers (2003) concluded that the direction of motion of the star with respect to its local ISM was within roughly 20° from the LOS to the star.

Distance estimates for WR 124 vary from 4.5 kpc (Pismis & Recillas-Cruz 1979) to 6.5 kpc (Nugis & Lamers 2000). The star has a terminal wind velocity of 710 km s^{-1} (van der Hucht 2001) and an upper limit for the mass loss rate of $1.3 \times 10^{-5} M_\odot$ yr^{-1} (Cappa et al. 2004). The stellar proper motion is (μ_α, μ_δ)(mas yr^{-1}) = (0.1 ± 2.0, −6.8 ± 2.0) based on the Tycho-2 Catalogue (Hog et al. 2000) and the catalogued heliocentric radial velocity is 194 ± 20 km s^{-1} (Wilson 1953).

In order to locate signs of the interaction between the stellar wind and the ISM, we observed the radio continuum and the H I distribution around the star. We also made use of available infrared data. In particular the H I data are crucial in establishing the large-scale (in arc-minutes) geometry around the star.

2. Observational data

2.1. λ 21 cm H I line emission

In order to image H I structures at all spatial frequencies, the region near WR 124 was observed with both the VLA and the Effelsberg radiotelescopes.

The Effelsberg data were obtained in August 1991. A $2° \times 2°$ region centered at the stellar position was observed. Within this region, the observed points were sampled at different spacings. The inner region, $1° \times 1°$ in size, has a grid spacing of $5'$ and is fully sampled, while outside this region the spacing is $10'$. The *HPBW* and main-beam efficiency at $\lambda \sim 21$ cm are $9'$ and 0.72, respectively. The velocity coverage is ~ 330 km s^{-1} and the velocity resolution 0.77 km s^{-1}. The rms noise level varies between 0.25 and 0.35 K in main-beam brightness temperature units. This scale was derived from observations of the IAU standard region S7 [$(l, b) = (132°0, -1°0)$] (Williams 1973). All profiles were corrected for stray radiation by applying the procedure outlined by Kalberla et al. (1980). The overall brightness temperature scale is accurate to 2%–3%.

The central region was also observed with the VLA in the D-array on 25 May 1999. The instrumental parameters are summarized in Table 1. Using DRAO application software, the single dish and the VLA data were then transformed to the $u - v$ plane, filtered in a complementary manner, and merged to provide an H I cube containing 127 images. The final angular and velocity resolutions are $46''5 \times 45''5$ at PA $16°6$ and 2.6 km s^{-1}, respectively.

2.2. VLA continuum

Radio continuum observations of M 1-67 at 8.5 GHz (3.6 cm) using the VLA in its D-array configuration were carried out on 12 November 2001. The field of view is $5'3$ and the bandwidth is 50 MHz. The on-source observing time was about 25 minutes to achieve a rms noise of ~ 0.08 mJy beam^{-1}. The observational parameters are summarized in Table 1. The data were edited, calibrated in both amplitude and phase and imaged following a standard procedure using AIPS tasks. No short spacing information was added to the interferometric image of M1-67 at 8.5 GHz.

2.3. Infrared

Near and far infrared images of the WR 124 region were retrieved from the *Midcourse Space Experiment* (MSX[1]) and IRIS[2] databases. MSX has carried out a survey of the entire Galactic plane within the range $|b| \leq 5°$ at six wavelengths from 4.2 to 21.3 μm. For most of the Galactic plane work, four of these bands, namely bands A (8.28 μm), C (12.1 μm), D (14.65 μm) and E (21.34 μm), are relevant. MSX produced images with an angular resolution of 19″ and an absolute astrometric accuracy

---

[1] The Infrared Processing and Analysis Center (IPAC) provides access to the MSX and IRAS images through the Infrared Science Archive at http://irsa.ipac.caltech.edu

[2] http://www.ias.fr/IRIS

Table 1. Observational parameters for VLA Data

Right ascension of the field center (J2000.0)	$19^h 11^m 30^s8$
Declination of the field center (J2000.0)	$16°51'38''$
Galactic longitude	$50°2$
Galactic latitude	$3°31$
VLA configuration	D
H I 21 cm line data	
FWHM of synthesized beam	$46''5 \times 45''5$
Position angle	$16°6$
Velocity coverage (LSR) (km s^{-1})	-162.3 to 162.3
Velocity resolution (km s^{-1})	2.6
rms noise (K)	0.3
Flux density calibrator	1331+305
Phase calibrator	J1925+211
Radio continuum data at 8.5 GHz	
FWHM of synthesized beam	$8''2 \times 7''7$
Position angle	$67°$
rms noise (mJy beam^{-1})	0.08
Primary flux density calibrators	3C48, 3C286
Secondary calibrator	1924+156

of $1''9$ (Egan et al. 1999; Price et al. 2001). The four MSX bandpasses are sensitive to different emission processes. Bands A and C (as well as the IRIS 12 μm band) may contain contributions arising from both fine-structure line emission and discrete PAH emission bands as well as continuum emission from dust at ~ 400 K. The emission in Bands C and E mainly arises from warm dust at ~ 100 K, it may also be contaminated by a [S III] fine-structure line emission at 18.71 μm (arising from H II regions of intermediate excitation) and by a broad 22 μm emission feature (Chan & Onaka 2000) (arising from dust in supernova remnants). IRIS images (Miville-Deschênes & Lagache 2005) are a new generation of IRAS images that benefit from a better zodiacal light subtraction, calibration, zero levels compatible with DIRBE and a better destriping. IRIS images have a lower angular resolution, typically around $4'$, than the IRAS ones.

To cover a large area towards WR 124, 1×1 deg^2 MSX and IRIS images centered at the optical position of WR 124 were downloaded from the archive node for scientific data sets from NASA's infrared projects (IRSA[1] site for short and the IRIS web site[2]). The images were further processed using the AIPS package. From an analysis of source-free regions located close to WR 124, the noise level of the MSX A, C, D and E bands were found to be 1.3, 19.2, 11.2 and 26.5 MJy sr^{-1}, respectively.

3. Results

3.1. H I distribution

The high-resolution fully sampled H I data cube provides a unique opportunity to investigate the H I distribution around WR 124. We inspected the entire H I cube, looking for signatures of the interaction of the stellar wind with the ISM in a region close to the stellar position. Since the work of van der Sluys & Lamers (2003) suggests that the stellar motion with respect to its local ISM is mostly along the LOS (receding), an H I deficiency centered approximately at the position of the star is expected. Indeed a structure possessing the characteristics expected for a star with a strong wind (e.g., a relative minimum in the H I brightness temperature distribution around the star surrounded by excess H I emission due to the swept-up gas) is observed in the velocity range from about 54 to 64 km s^{-1} (LSR). The corresponding channel images are shown in Fig. 1. In order to
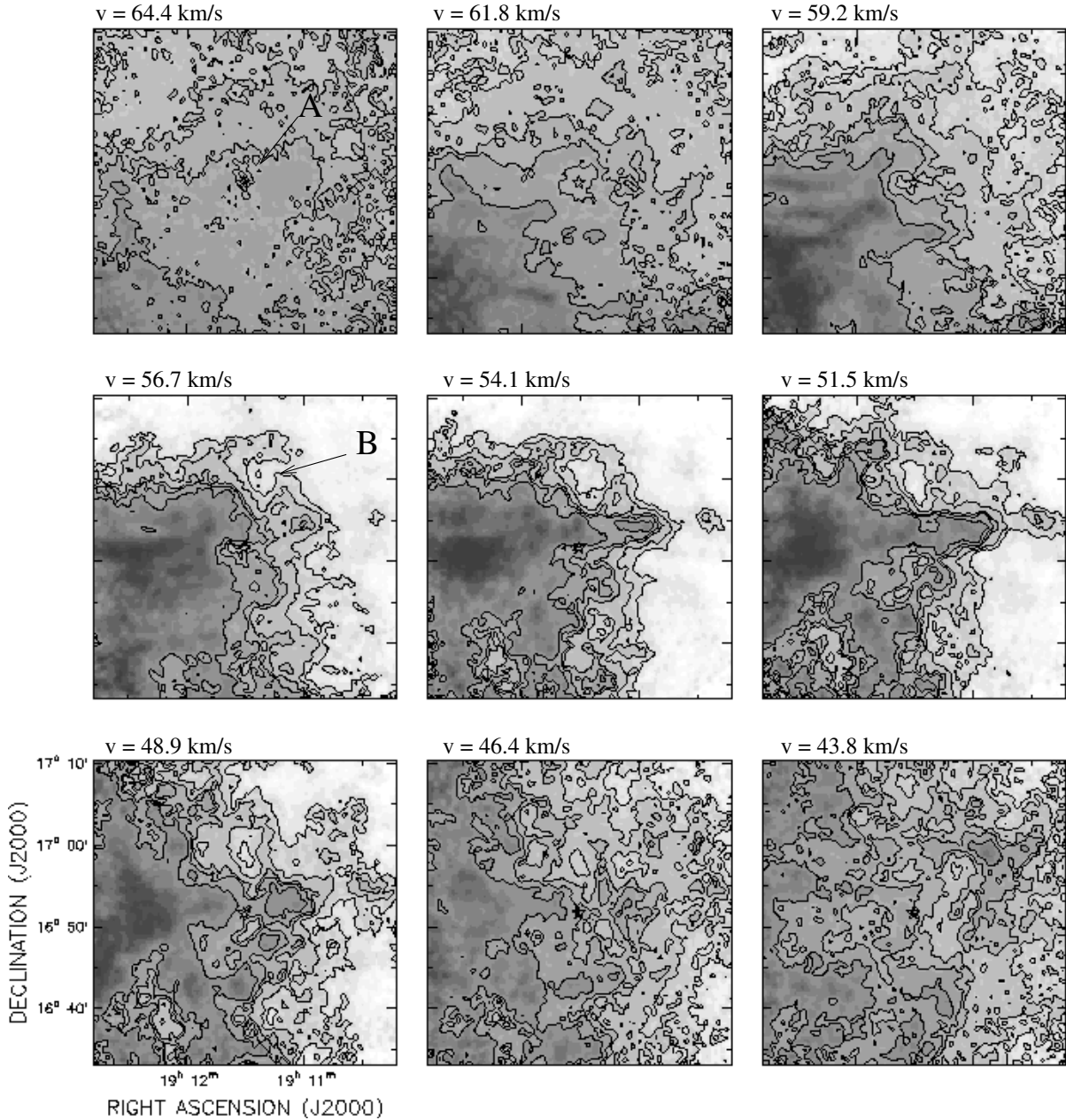
Fig. 1. Grey-scale images showing the H I gas distribution in the velocity range 64.4 to 43.8 km s^{-1} observed with the VLA and the 100 m Effelsberg telescope. The position of WR 124 is indicated by a star symbol. Velocity resolution is 2.6 km s^{-1} and the spatial resolution is $46\rlap{.}''5 \times 45\rlap{.}''5$ with a PA of $16\rlap{.}°6$. The LSR velocity of each image is indicated in the top left corner. Letters A and B indicate the cavities described in the text. Contour levels with respect to the average over each image are $-13, -8, -3, 0$ and 5 K. Noise is 0.3 K or 1.05 mJy beam^{-1}.

facilitate their display, the images are shown with their mean level subtracted. At $v = 64.4$ km s^{-1} the star is seen projected close to the center of a small H I depression (designated by the letter A) surrounded by weak H I emission. This minimum gets larger as we move towards lower velocities, being better defined at 61.8 km s^{-1} and barely visible at 54.1 km s^{-1}.

In the velocity range from 56.7 to 51.5 km s^{-1} a strong and nearly horizontal bar-like feature crosses the image near $\delta \sim 16°55'$. This structure probably distorts the northern part of the H I depression. In Fig. 2 the distribution of the mean brightness temperature averaged over the velocity range from 56.7 to 61.8 km s^{-1} is shown. A well-defined H I cavity near the position of the star and the confusing presence of the bar-like feature mentioned above are apparent.

3.2. The ionized gas

Figure 3 shows the VLA radio continuum image at 3.6 cm and the HST-WFPC2 Hα image of M 1-67 obtained by Grosdidier et al. (2001). The spatial extent of the emission at optical and radio wavelengths is comparable. The radio image of M1-67 displays a clumpy structure on a scale of a few arc seconds. No clear shell-like appearance is obvious either in the optical or the radio image. The flux density at 8.5 GHz is 205±10 mJy.

Previous radio images of M 1-67 include Westerbork observations by Israel & Felli (1976) at 21 cm ($HPBW \sim 46''$) and by Felli & Perinotto (1979) at 6 cm ($HPBW \sim 11''$). With the new high sensitivity VLA image (Fig. 3a), the fainter outer regions of M1-67 were detected, including the radio counterparts of the outer areas observed in the optical range. Table 2 summarizes
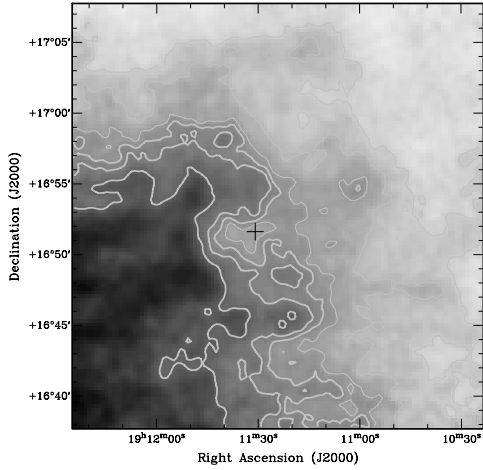
Fig. 2. Average H I brightness temperature within the LSR velocity interval 54.1 to 61.8 km s^{-1}. Contour levels with respect to the average over the image (28 K) are -10, -6, -2, 0, 2 and 6 K. The cross indicates the position of WR 124.

the existing flux density determinations of M1-67. To derive the spectral index we discarded flux density measurements with signal to noise ratio lower than 3. A weighted least-square fit to the data yielded a spectral index $\alpha = -0.06 \pm 0.04$ ($S_\nu \sim \nu^\alpha$). Within these errors, the radio flux densities are consistent with a thermal spectrum. The large spread of values, particularly around 5 GHz, may arise in : i) different procedures used to remove the presence of background/foreground emission, ii) observations with different sensitivity (those with high rms noise will mask low level radio emission), and iii) different absolute calibrations.

3.3. Infrared emission

In Fig. 4 the MSX emission in the range 8 to 21 μm is shown. The infrared emission slightly departs from circular symmetry in bands A and E, has an incomplete shell morphology in band C, and is barely visible in band D. The extent of the IR emission in band A is similar to the emission observed in the Hα and 8.5 GHz radio continuum images. In all bands WR 124 is slightly offset from the peak of emission. Based on the measured flux densities quoted in Table 3 it is clear that the grains responsible for the emission in the 60 and 100 μm IRIS images cannot be responsible for the emission observed in the MSX bands. The lack of spatial correlation between bands A and D may imply that the emission in band A is dominated by fine-structure line emission and/or infrared emission from PAH molecules. Detailed modeling beyond the scope of this paper is needed to disentangle the main contributing agents.

4. Discussion

4.1. H I structures

For a flat Galactic rotation model with $R_\odot = 7.6$ kpc (Eisenhauer et al. 2005) and $\Theta_\odot = 214$ km s^{-1} (Kothes & Dougherty 2007), the highest positive LSR radial velocity (i.e. the velocity at the tangent point) permitted along the LOS (for $l = 50°.2$) is about 50 km s^{-1}. The tangent point in this direction is at a distance of about 5 kpc from the Sun. This means that strictly speaking there should be no H I gas with velocities greater that 50 km s^{-1}. However, H I emission is observed up to 65 km s^{-1}. Moreover, as was described in Sect. 3.1, an H I cavity, named cavity A,

is observed near the stellar position in the LSR velocity range from 64 to 54 km s^{-1}. In order to reconcile the observed radial velocity with the Galactic rotation model, we must allow the rotation curve to have a small peculiar velocity in this direction. Assuming for the tangent point a velocity of 65 km s^{-1}, a kinematic distance of 5 kpc is inferred for cavity A. This H I distance is in good agreement with previous distance determinations for the star (~5 kpc, Pismis & Recillas-Cruz 1979; Nugis & Lamers 2000). Hereinafter a distance of 5 kpc for both the star and the H I feature is adopted.

Given that WR 124 is seen projected on cavity A and both are likely at the same distance from the Sun, we believe that cavity A is a consequence of the stellar wind of WR 124. However, we can not completely rule out the possibility that the spatial agreement between cavity A and WR 124 arises from a chance coincidence. In order to rule out a "by chance" origin for cavity A, we have followed the procedure described by Arnal (1992), who analyzed the H I distribution around several WR stars using Effelsberg data. Given the difference between the Effelsberg and VLA beams (9′ and ~1′, respectively), the histograms given in his paper do not apply. For this reason, we have used H I data obtained from the VLA Galactic Plane Survey (VGPS, Stil et al. 2006) to reproduce his work. We have chosen a region near WR 124 (49°.0 ≤ l ≤ 51°.5, 0°.6 ≤ b ≤ 1°.9 and 44 ≤ v ≤ 72 km s^{-1}) where no massive stars or SNR are known to be present. In this case any H I holes are just random structures and will be referred to as random holes. Because of the turbulent nature of the H I on small spatial scales, the images were first smoothed to a spatial resolution of 2′, i.e., about half the diameter of cavity A. Figure 5 shows two histograms, one corresponding to the area and the other to the velocity extent of the observed random holes.

Taken at face value, these histograms show that random H I holes peak at an area of about 75 arcmin^2 (equivalent to a diameter of about 10′ for a circular hole). These random holes also have a relatively small velocity extent (peak near 5 km s^{-1}) compared to that of cavity A. Using the two histograms to evaluate the probability that cavity A has by chance the size and velocity extent observed, we deduce a combined probability of about 0.01.

The relatively small size of cavity A, compared to H I cavities identified around other WR stars (Cappa et al. 2003), is of significance and deserves further attention. The cavity radius at maximum extent is only about 2′.5 which, at a distance of 5 kpc, corresponds to about 3.6 pc. For the sake of comparison, the radius of a classical stellar wind bubble around a star at rest with respect to the ISM is given by (Castor et al. 1975; Weaver et al. 1977) $R(t) = 28 (L_{w36} t_6^3 n_o^{-1})^{1/5}$ pc, where n_o is the undisturbed ISM number density, $L_w = \frac{1}{2}\dot{M}v_\infty^2$ is the wind luminosity, $L_{w36} = L_w/10^{36}$ erg s^{-1}, t is the time over which the stellar wind has been acting upon the surrounding ISM, and $t_6 = t/10^6$ yr. For any reasonable value of the parameters, $R(t)$ considerably exceeds the observed radius of cavity A.

However, for a very fast hypersonically moving star such as WR 124, the actual appearance of the ensuing structure is not described by the symmetric structure characterized by the above equation for $R(t)$. Contrary to the standard theory of stellar wind bubbles, which describes the evolution in time of the radius, and velocity of a closed structure surrounding a massive star with a strong stellar wind, the bow shock created by a supersonically moving star is a stationary time-independent paraboloid structure (Wilkin 1996; Raga et al. 1997). The scale of this bow shock depends not only on the wind velocity and mass loss rate but also on the peculiar velocity of the star. Furthermore the orientation
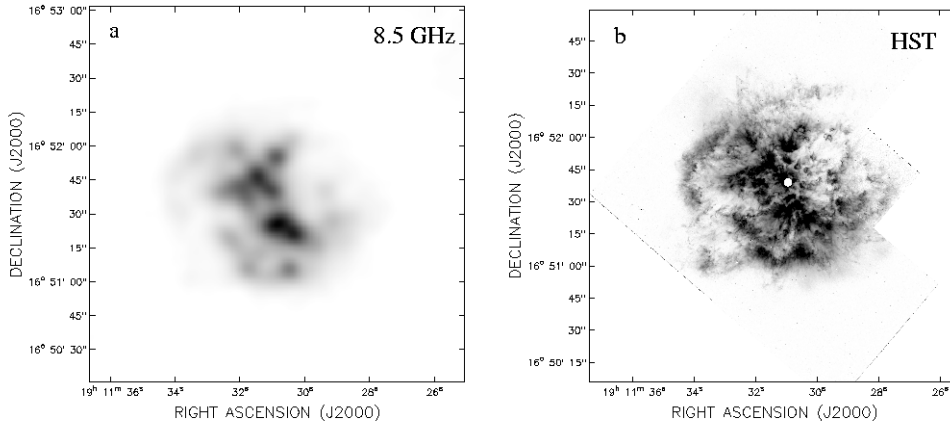
Fig. 3. a) Radio continuum image of M1-67 at 8.5 GHz with a resolution of ~8″. The grey scale goes from 0 to 7 mJy beam^{-1} (dark grey). **b)** HST-WFPC2 Hα image of M 1-67 obtained by Grosdidier et al. (2001). Resolution is ~0.″2.

Table 2. Flux density estimates of M1-67.

ν (MHz)	S_ν (mJy)	HPBW	Reference[a]
430	340 ± 50	10′	IF
1415	225 ± 35	24.″6 × 84.″9	IF
1420	230 ± 46	9.′4	RR
1465	214 ± 10	45.″0	CK
2695	210 ± 21	4.′3	FF
2700	290 ± 100	8.′1	IF
3240	160 ± 35	8.′4	IF
4900	196 ± 18	3.′7	GB6
4900	153 ± 30	6″ × 40″	FP
4995	320 ± 50	6′	IF
4995	237 ± 25	4.′5	IF
6630	200 ± 24	4′	IF
8460	205 ± 10	8.″2 × 7.″7	This paper
10 630	179 ± 89	2.′7	IF
15 500	250 ± 60	2.′2	IF
15 500	130 ± 60	2.′2	IF

^{a} IF: Israel & Felli (1976); FP: Felli & Perinotto (1979); RR: Reich et al. (1990); CK: Condon & Kaplan (1998); FF: Fürst et al. (1990); GB6: Condon et al. (1994)

of the bow shock symmetry axis is determined by the direction of the relative velocity between the star and its local ISM.

To assess the possible importance of the component of motion of WR 124 on the sky, we use the value of inclination i given by van der Sluys & Lamers (2003), $i \approx 20°$, and take 200 km s^{-1} as the approximate spatial velocity of WR 124 with respect to its local ISM. The tangential component of velocity is thus 200 sin i km s^{-1} ≈ 68 km s^{-1}, a significant number corresponding to an approximate angular displacement on the sky (mostly towards southern declination) of about 0.″8 t_6. Based on this qualitative argument, it is not justifiable to simply approximate the motion of the star as mostly receding along the LOS and some H I signature on the plane of the sky should be looked for.

4.2. A simple bow shock model

The structure of interstellar bubbles (IB) created by the powerful winds of massive stars has been well modeled (e.g. Castor et al. 1975; Weaver et al. 1977). For a star at rest with respect to its ambient interstellar gas, these models predict that the corresponding IB is spherical in shape with the star projected near its center. However, as the stellar spatial velocity increases, the idealized spherical structure of the IB is distorted as compared to that formed by a low velocity star (Weaver et al. 1977). If the stellar velocity becomes supersonic, a bow shock structure develops. This structure is axisymmetric along the direction of the stellar spatial velocity and can be approximated by a paraboloid of revolution. An analytic solution for its shape was derived by Wilkin (1996). In this model the shape of the bow shock is determined by the balance between the ram pressure of the wind, the ram pressure of the ambient medium in the reference frame of the star, and the flow of momentum along the surface of the bow shock. This model provides a simple and useful description of the shape of the bow shock, the distribution of the surface density and the gas velocity along its surface. The star is assumed to move with a constant velocity v_{ism} relative to an ISM of uniform density ρ. The isotropic stellar wind has mass loss rate $\dot{m}_w$ and constant terminal speed V_w, yielding a paraboloid cometary structure with the stellar velocity vector as symmetry axis. In this idealized model, the bow shock is at a distance $R(\theta)$ from the star, where $R(\theta) = l_o \csc \theta \sqrt{3(1 - \theta \cot \theta)}$ and θ is the polar angle measured from the symmetry axis with the star at the coordinate origin (see Fig. 6). The bow shock stand-off distance ($\theta = 0°$) sets the length scale and is given by $l_o = \sqrt{\dot{m}_w V_w/(4\pi \rho v_{ism}^2)}$. Although Wilkin's model uses a thin shell approximation, several numerical simulations of bow shocks (Raga et al. 1997; Arthur & Hoare 2006) have shown that this simple model traces relatively well the average position of the bow shock. The main advantage of using this simple model is that the number of variable parameters is kept to a minimum, thus allowing one to focus on identifying dominant effects rather than trying to precisely reproduce generally complex observational data.

The tridimensional bow shock surface is obtained by rotating Fig. 6 by 2π about the symmetry axis. The orientation is given by specifying the inclination of the axis with respect to the LOS (angle i) and the position of the projected axis on the plane of the sky (position angle ϕ measured counter-clockwise from north). For an image in equatorial coordinates, the angles i and ϕ are related to the stellar velocity by the relations $i = \arccos(v_r/v_{ism})$, $\phi = \arctan(v_l/v_b) - \epsilon$ where v_r, v_l, v_b and v_{ism} are the radial velocity, velocity in the longitude and latitude directions and total stellar velocity with respect to the local ISM at the position of
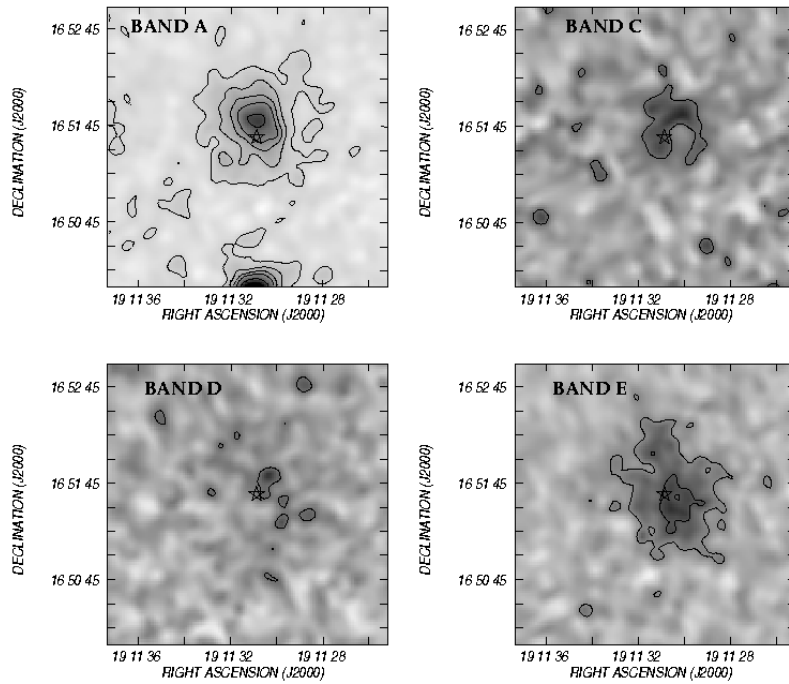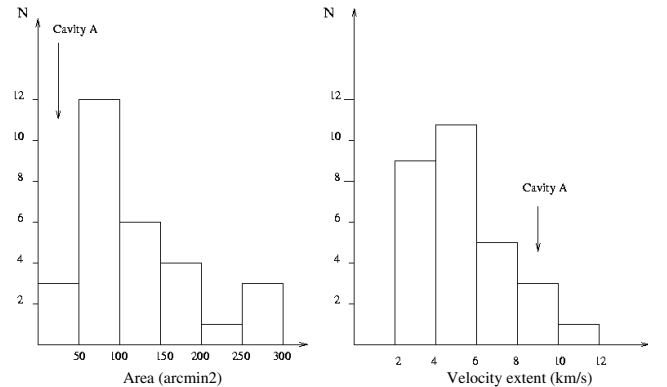
Fig. 4. MSX images towards WR 124 (star symbol). The lowest contour level represents a noise level of 4.5σ for band A and 3σ for the others bands. Low intensity regions are indicated by light greys. *Top left panel*: 8.28 μm (band A) emission. The grey scale range is -2 to 35 MJy sr^{-1}. The contour lines are 6, 10, 14, 18, 26, 34, 42 and 50 MJy sr^{-1}. *Top right panel*: band C image (12.1 μm). The grey scale spans -75 to 130 MJy sr^{-1}. The contour line is 57.7 MJy sr^{-1}. *Bottom left panel*: band D image at 14.65 μm. The grey scale range is -47 to 80 MJy sr^{-1}. The contour line is 33.6 MJy sr^{-1}. *Bottom right panel*: band E image at 21.3 μm. The grey scale covers the range -130 to 260 MJy sr^{-1}, contour lines are 79.5 and 159.0 MJy sr^{-1}.

Table 3. MSX and IRIS integrated flux densities.

Wavelength (μm)	Total flux (Jy)
8.28	0.75 ± 0.15
12.0	2.0 ± 0.3
12.1	2.4 ± 0.5
14.7	1.5 ± 0.9
21.3	12.9 ± 3.7
25.0	25.2 ± 0.6
60.0	59.4 ± 1.7
100.0	20.0 ± 1.7

Fig. 5. Histograms of the random H I holes area and velocity extent identified in a region near the stellar position. The arrows indicate the area and velocity extent observed for cavity A.

the star, respectively. The angle ϵ is the angle between a line of constant declination and a line of constant Galactic latitude measured counter-clockwise from the positive l axis. Detailed transformation equations leading to i and ϕ can be found in van der Sluys & Lamers (2003) (note however that our definition of ϕ differs from theirs and that the sign of the $w_\odot$ term in their Eq. (19) must be reversed).

As a consequence of the stellar velocity, the incoming ISM is shocked, ionized and flows tangentially in a thin layer along the bow shock surface (i.e., along the cone shown in Fig. 6; see also Fig. 1 of Wilkin 1996). Wilkin (1996) gives an analytic solution for the velocity of the shocked gas at all points on the shell. It is unclear whether the shocked matter can ever recombine to form a neutral H I layer and, if it does, where this takes place. One expects this to happen significantly far downstream from the star, where the tangential velocity has become negligible. The primary H I signature of a bow shock is thus likely to be that of an elongated H I cavity having a conical structure aligned with the projected direction of motion of the star (i.e., the empty interior

within the bow shock surface). It is important to mention that in a realistic ISM, the conical structure may be broken or distorted by the presence along the same LOS of unrelated (with respect to the bow shock) H I features.

4.3. The case of WR 124

Keeping in mind van der Sluys & Lamers' (2003) estimate for the approximate direction of the stellar velocity on the sky, we inspected the H I distribution looking for signatures of a bow shock. Figure 1 shows that another H I minimum (indicated as B) is observed at 56.7 km s^{-1}. This H I depression is centered at $(\alpha, \delta) \sim (19^{\rm h}11.3^{\rm m}, 17\overset{\circ}{.}0)$, i.e. $\sim 10'$ to the north of the stellar
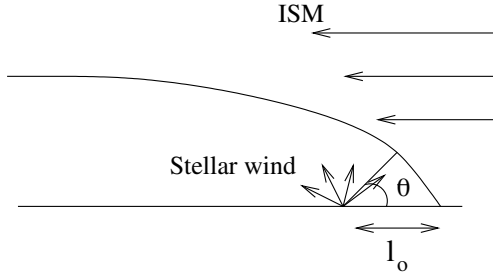
Fig. 6. Schematic side view representation of the geometry of the bow shock model. The horizontal axis represents the symmetry axis of the bow shock and l_o is the stand-off distance.

position and is present to velocities about 46 km s^{-1}. This cavity is elongated in a general N-S direction.

The elongated large-scale horizontal structure crossing the field near $\delta \sim 16° 55'$ appears to be responsible for the fact that cavities A and B appear separated and/or distorted, rather than forming a smooth structure like that suggested by Fig. 6. Within the bow shock picture, cavity A corresponds to the approximate position of the apex, while cavity B can be interpreted as corresponding to the rear part of the bow shock.

The positions of cavities A and B can be used to correctly orient the structure shown in Fig. 6 so that it fits the H I data for WR 124. This procedure consists of obtaining estimates of the angles i and ϕ. As mentioned before, van der Sluys and Lamers (2003), using the Fabry-Perot Hα observations of Grosdidier et al. (2001), had obtained values of $i = 20°$ and $\phi = 175°$ (our definition of ϕ). It is worth noting however, that their results are based on optical observations of a region of ionized gas covering only about $2'$ on the sky. In a sense, the optical data only sample the exact region of the apex while our neutral hydrogen images cover a much wider field of some $50'$ in diameter and sample the more global bow shock structure. As the main goal is to find a general fit of the "large-scale" H I data (basically an absence of H I within a given volume) to a bow shock model, we wish to establish the range of parameters allowed by the observational data (essentially the proper motions). Using a radial velocity of 194 ± 20 km s^{-1} (Wilson 1953), a proper motion $(\mu_\alpha, \mu_\delta) = (0.1 \pm 2.0, -6.8 \pm 2.0)$ mas yr^{-1} (Tycho-2 Catalogue) and assuming a distance of 5 ± 1.5 kpc, following van der Sluys & Lamers (2003) we obtain $v_r = 162 \pm 20$ km s^{-1}, $v_l = -15 \pm 81$ km s^{-1}, $v_b = -81 \pm 53$ km s^{-1}, and $v_{ism} = 182 \pm 31$ km s^{-1}, from which we deduce $i = 27° \pm 24°$ and $\phi = 128° \pm 55°$ ($\epsilon = 62°.7$ for WR 124). If instead Hipparcos proper motions are used $(\mu_\alpha, \mu_\delta) = (0.01 \pm 2.93, -10.29 \pm 1.90)$ mas yr^{-1}, we obtain $v_{ism} = 219 \pm 58$ km s^{-1}, $i = 42° \pm 18°$ and $\phi = 155° \pm 34°$. These estimates, solely based on the observed radial velocity and proper motions, suggest that the angles should lie in the approximate range $5° \leq i \leq 60°$ and $70° \leq \phi \leq 190°$. The stand-off distance, assuming a typical value of 1 cm^{-3} for the undisturbed ambient number density, is $0.8 \leq l_o \leq 1.0$ pc.

Taking into account the large allowed range for i and ϕ, mostly as a consequence of the errors in the proper motions, we derive the angles i and ϕ that best fit our H I observations. Under the assumption that cavities A and B are part of the same bow shock structure, the angles obtained are $i = 30°$ and $\phi = 170°$.

The corresponding 3D rotated structure for $l_o = 1$ pc is presented in the bottom right corner of Figs. 7a,b, where the observed H I distribution at $v = 61.8$ and 54.1 km s^{-1} is shown. As mentioned in Sect. 3.1, the presence of a horizontal structure at $\delta \sim 16°55'$ precludes the observation of the H I minima that would correspond to intermediate parts of the paraboloid, hence

giving the false impression that cavities A and B are unrelated to each another. Keeping in mind that a realistic inhomogeneous ambient ISM is likely to result in significant deviations from the ideal model, the 3D bow shock structure shown as an inset in Figs. 7a,b indicates that the bow shock model is consistent with the H I observations. It is implicit to our interpretation of the H I data that the observed holes (cavities A and B) arise as a consequence of the hollow structure of a bow shock that is being viewed from its rear part, along a LOS that makes a small angle with respect to the symmetry axis of the parabolic shape defining an ideal bow shock structure. This picture is also consistent with a scenario where the ionization front generated by the Lyman continuum photons emitted by WR 124 is trapped within the stellar wind shock. If this were not the case, the H II region would be much larger than the bow shock (Raga et al. 1997). In our scheme, the radio continuum, the infrared, and the Hα emission arise from a small region circumscribed to the apex of the bow shock structure.

Along the same line of reasoning we can even go as far as to argue that a much larger H I cavity than the one observed centered on WR 124 would have been incompatible with the highly supersonic motion of the star and the unavoidable formation of a bow shock structure. Furthermore the existence of an H I deficiency in the general direction from which the star is incoming, strengthens the probability argument against chance coincidence. A simple probability argument consists of estimating the combined probability that, simply by chance, WR 124 is seen superposed on cavity A and that cavity B is seen in a direction (as seen from the position of WR 124) corresponding to the incoming direction of the star on the sky (estimated on the basis of the size subtended by cavity B as seen from WR 124). This simple argument yields a small combined probability of less than 0.01.

Concerning the kinematics of the H I gas, it is important to emphasize that the observed velocities are not expansion velocities (as is the case for spherical bubbles). The difference in velocity between cavity A and B can be explained in terms of the expected velocity dispersion of the H I gas (4.2 km s^{-1}, Blitz & Spergel 1991) as well as turbulent motions. Cavities A and B can be considered as part of the same structure having a centroid velocity of ~ 55 km s^{-1}.

The fact that cavity B is not open to the north can be interpreted as an indication that the bow shock cavity has begun to close behind the star. For $i = 30°$ and $\phi = 170°$, the distance traveled by the star from the northernmost part of cavity B is $D_* = 23$ pc. As a first rough approximation the cavity can be assumed to close on a sound-crossing timescale. The sound speed c_s required for the cavity to close on the timescale it takes the star to travel the distance D_* is $c_s \approx 45$ km s^{-1}. This sound speed corresponds to a gas temperature of $\sim 20 \times 10^4$ K, consistent with what may be expected for hot stellar wind gas. From the form $R(\theta)$ of the cavity, we can estimate the transverse (i.e., perpendicular to the symmetry axis) dimension of the cavity d_t at the distance D_*. We obtain $d_t \sim 12$ pc, corresponding to an angular width of $d_t \sim 30^s$ (or $8.'3$) at 5 kpc. This value is in good agreement with the width of the northernmost part of cavity B. The corresponding angle θ (see Fig. 6) is about 150°. Although it is clear that the model will break down at very large distances downstream, Raga et al. (1997) and Arthur & Hoare (2006) obtained the same angle in their numerical simulations. In fact, Fig. 4 of Raga et al. (1997) and Fig. 22 of Arthur & Hoare (2006), show their numerical solutions behave generally as expected by the analytical model out to angles of about 145°. The simulation of Arthur & Hoare (2006) shows a structure more open than the analytical model and the shock at the apex more
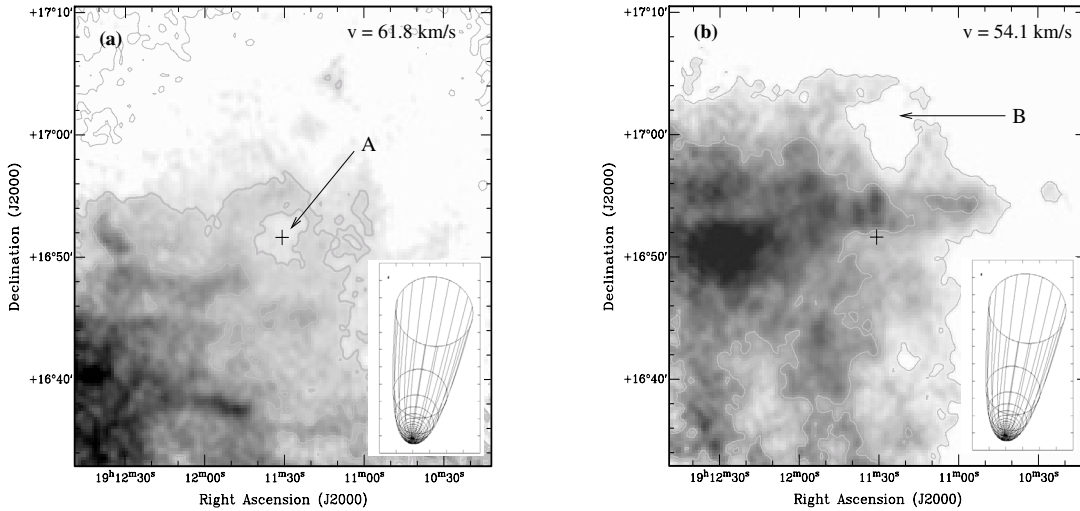
Fig. 7. a) H I emission distribution at $v = 61.8$, where cavity A is best delineated. **b)** H I emission distribution at $v = 54.1$ km s^{-1}, where cavity B is best delineated. In both panels contour levels are -10, 0 and 5 K. The cross marks the position of WR 124. The 3D bow shock structure for $i = 30°$ and $\phi = 170°$ is shown in the bottom right corner.

distant by about a factor of 1.5. The simulation of Raga et al. (1997) was for a fast (100 km s^{-1}) star moving in a low density medium (1 cm^{-3}) whereas that of Arthur & Hoare (2006) is more typical of cometary H II regions (low velocity of 20 km s^{-1} and high density of 6000 cm^{-3}). These simulations give us confidence that the use of Wilkin's analytical model is justified.

Finally it is encouraging that the fitting of a simple minded bow shock model to the H I images ($\sim 50'$ in diameter) leads to values of i and ϕ (30° and 170°, respectively) which are in good agreement with the values (20° and 175°, based on our definition of ϕ) obtained by van der Sluys & Lamers (2003) using a completely different database and involving the same simple model but on a considerably smaller angular scale.

4.4. Ionized gas and dust in M1-67

The physical parameters derived for the ionized gas in the nebula are summarized in Table 4. The ionized mass M_i and electron density n_e were obtained from the classical expressions (Mezger & Henderson 1967) for a sphere of 55″ in radius ($R_s = 1.3$ pc at 5 kpc) with uniform electron density n_e and an electron temperature of 6200 K (Esteban et al. 1991). The adopted values coincide with those by Grosdidier et al. (1998), although the distances are slightly different. We give separate estimates corresponding to different values of the volume filling factor f. The case $f = 1$ is unrealistic as it is clear from Fig. 3a that the plasma is quite clumpy. The bow shock is not a uniformly filled sphere but is better modeled as a hemispherical shell of radius R_s and thickness βR_s with β in the range 0.1 to 0.2. The hot plasma covers only 40 to 60% of the volume of this hemispherical shell. The last two lines of Table 4 give the values of n_e and M_i corresponding to filling factors between 0.05 and 0.15. Our estimates of n_e and M_i for $f = 0.05$ are consistent with the values derived by Grosdidier et al. (1998) on the basis of the HST Hα image (Fig. 3b).

The small physical size of the continuum nebula suggests that it corresponds to a limited region near the head of the bow shock where the surface density and hence emissivity is maximum (e.g., Mac Low et al. 1991; Van Buren et al. 1990). The fact that the structure observed at radio continuum, optical and infrared wavelengths does not conform to the expected one

Table 4. Main parameters derived from the radio continuum data at 3.6 cm for an assumed distance d of 5 kpc.

Parameter	Value
Flux density $S_{3.6\ cm}$	205 ± 10 mJy
Emission measure EM	1.3×10^4 pc cm^{-6}
Angular semi-axis	$\sim 55''$
Linear radius	~ 1.3 pc
rms electron density n_e ($f = 1.0$)	140
Ionized mass $M_i{}^a$ ($f = 1.0$)	22.5 $M_\odot$
Filling factor f	0.05–0.15
Electron density n_e	630–360 cm^{-3}
Ionized mass $M_i{}^b$	5–9 $M_\odot$

^{a} Including a factor of 1.27 for singly ionized He
^{b} Including a factor of 1.27 for singly ionized He

(namely an arc-like structure on the plane of the sky, see Fig. 1 of van Buren et al. 1990) has to do with the direction of motion of WR 124, that is is almost along the LOS. Under these conditions, projection effects render impossible the detection of the classic arc-like geometry which would be produced by a star mainly moving on the plane of the sky.

It is also evident from Fig. 3a that the radio continuum emission is highly irregular on scales probed by the VLA 3.6 cm observations. The origin of these irregularities is uncertain. On the basis of detailed abundance analysis (Esteban et al. 1991), the ionized mass has been inferred to consist mostly of ejecta. The ionized mass derived from the radio continuum data is consistent with this conclusion. As mentioned by van der Sluys & Lamers (2003), because the outbursts responsible for the nebula occur inside the bow shock, the ejecta collide with it and are then dragged along the bow shock surface, eventually adopting its velocity. Depending on the relative momentum of the outburst and of the wind-ISM shock, the outburst may adopt the geometry of the bow shock or, in an extreme case, distort it severely. We see structures down to the VLA resolution limit ($\approx 8''$) corresponding to a linear scale $l \approx 0.19$ pc at a distance of 5 kpc. These structures could correspond to irregularities of the bow shock surface (perhaps caused by inhomogeneities in the ISM) or alternatively to irregularities in the angular distribution of the

stellar wind. The HST image of Grosdidier et al. (2001) (Fig. 3b) shows that irregularities are in fact present on scales much smaller than those probed by the radio observations.

The data of Table 2 (see Sect. 3.2) are consistent with a thermal spectrum, which is the norm for stellar wind structures. However, a significant proportion of stellar wind objects also exhibit non-thermal radio emission. A case of particular interest is that of colliding-wind binaries (Eichler & Usov 1993) where the non-thermal emission is shown to arise at the point of ram pressure balance between the two stellar winds (Dougherty & Williams 2000; Dougherty et al. 2005). One might then ask whether a non-thermal component could be present in the WR 124 nebula. Such emission is clearly negligible if one considers emission integrated over the entire structure (Table 2). The apex of the bow shock would seem the ideal place to look for non-thermal radio emission. However, in order to look for possible spectral index variations, a higher-resolution radio image would be needed at a frequency sufficiently different from our own image.

Since the radio continuum image is free from extinction by dust, the morphological agreement between the VLA and HST images suggests a relatively low and rather uniform extinction across the nebula, which in turn suggests that ionized gas and dust are well mixed, and/or the presence of dust beyond the location of the ionized material. This last suggestion is also consistent with the fact that we are observing M1-67 through the major symmetry axis of the paraboloid.

As for dust emission, we integrate the energy distribution given in Table 3 and obtain the infrared luminosity of the nebula $L_{IR} \simeq 3.8 \times 10^3 \, L_\odot$. Under the assumption that the 60 and 100 μm emission is mostly due to radiatively heated dust grains, by fitting a modified Planck function of the form $\nu^m \, B_\nu(T_d)$) to the flux densities at 60 and 100 μm, where the first term accounts for the frequency dependence of the grain emission, we derive a mean dust temperature $T_d = 100 \pm 13$ K (for $m = 1$) and $T_d = 70 \pm 6$ K (for $m = 2$). The high T_d values merely reflect the fact that the observed feature is much stronger at 60 μm than at 100 μm, a behavior typical of bow shocks (van Buren & McCray 1988).

The high ($\sim$200 km s^{-1}) peculiar velocity of WR 124 implies the presence of a strong shock, particularly at the apex of the bow shock. This may lead to the selective (i.e., with respect to size) destruction of dust grains (Whittet 2003, p. 288) and to the collisional heating of the grains (Dwek 1987; Arendt 1989). Both factors are likely to significantly affect the intensity (hence morphology) and frequency dependence (dust temperature) of the observed IR emission.

5. Conclusion

In this work we have presented new high resolution radio data in the environs of WR 124. These data have allowed us to analyze the effects of the interaction between the stellar wind and the ISM surrounding WR 124. The runaway nature of the star is fundamental in interpreting and understanding the observations. From the analysis of the H I distribution, two cavities (named cavity A and cavity B) were identified as possibly related to the star. Both cavities are observed at LSR velocities of about 55 km s^{-1}. While cavity A is observed with WR 124 projected inside it, cavity B is located 10′ to the north of the stellar position. There is convincing evidence that these two apparently disconnected H I cavities are in fact part of the same bow shock structure caused by the star's supersonic motion.

From the continuum data, the new radio image together with past data obtained with a number of radio telescopes are consistent with a purely thermal emission process, as is the case for the majority of ring nebulae around massive stars (Cappa et al. 2003). Because of the particular viewing geometry in the present case, the radio continuum image represents essentially a snapshot picture of the ionized gas in the immediate vicinity of the forward bow shock cone associated with the supersonic motion of WR 124 through its local ISM. The radio morphology has been shown to be extremely similar to the optical one, suggesting that the ionized gas and the dust are well mixed and/or the dust is located beyond the ionized material.

The dust temperature deduced from the 60 μm and 100 μm images ($T_d \sim 70-100$ K) and the brighter 60 μm emission are in agreement with previous observations of bow shocks (van Buren & McCray 1988). The MSX images show that the IR morphology changes dramatically between different wavelengths. We interpret these results as indicating that the physical conditions in bow shocks associated with supersonically moving stars are significantly different from those encountered in the standard stationary stellar wind shocks.

References

Arendt, R. G. 1989, ApJS, 70, 181
Arnal, E. M. 1992, A&A, 254, 305
Arthur, S. J., & Hoare, M. G. 2006, ApJS, 165, 283
Bertola, F. 1964, PASP, 76, 241
Blitz, L., & Spergel, D. N. 1991, ApJ, 370, 205
Cappa, C. E., Arnal, E. M., Cichowolski, S., Goss, W. M., & Pineault, S. 2003, in A massive star odyssey: from main sequence to supernova, ed. K. A. van der Hucht, A. Herrero, & C. Esteban (PASP), IAU Symp., 212, 596
Cappa, C. E., Goss, W. M., & van der Hucht, K. A. 2004, AJ, 127, 2885
Castor, J., McCray, R., & Weaver, R. 1975, ApJ, 200, L107
Chan, K. W., & Onaka, T. 2000, ApJ, 533, L33
Crawford, I. A., & Barlow, M. J. 1991, A&A, 249, 518
Condon, C. C., & Kaplan D. L. 1998, ApJS, 117, 361
Condon, J. J., Broderick, J. J., Seielstad, G. A., Douglas, K., & Gregory, P. C. 1994, AJ, 107, 1829
Dougherty, S. M., & Williams, P. M. 2000, MNRAS, 319, 1005
Dougherty, S. M., Beasley, A. J., Claussen, M. J., Zauderer, B. A., & Bolingbroke, N. J. 2005, ApJ, 623, 447
Dwek, E. 1987, ApJ, 322, 812
Egan, M. P., Price, S. D., Moshir, M. M., Cohen, M., & Tedesco, E. 1999, The Midcourse Space Experiment Point Source Catalog Version 1.2 Explanatory Guide. Air Force Research Laboratory Technical Report, AFRL-VS-TR 1999-1522
Eichler, D., & Usov, V. 1993, ApJ, 402, 271
Eisenhauer, F., Genzel, R., Alexander, T., et al. 2005, ApJ, 628, 246
Esteban, C., Vilchez, J. M., Smith, L.J., & Manchado, A. 1991, A&A, 244, 205
Felli, M., & Perinotto, M. 1979, A&A, 76, 69
Fürst, E., Reich, W., Reich, P., & Reif, K. 1990, AAS, 85, 805
Grosdidier, Y., Moffat, A. F. J., Joncas, G., & Acker, A. 1998, ApJ, 506, L127
Grosdidier, Y., Moffat, A. F. J., Blais-Ouellette, S., Joncas, G., & Acker, A. 2001, ApJ, 562, 753
Hog, E., Fabricius, C., Makarov, V. V., et al. 2000, A&A, 355, L27
Israel, F. P., & Felli, M. 1976, A&A, 50, 47
Kalberla, P. M. W., Mebold, U., & Reich, W. 1980, A&A, 82, 275
Kothes, R., & Dougherty, S. M., 2007, A&A, 468, 993

Mac Low, M.-M., Van Buren, D., Wood, D. O. S., & Churchwell, E. 1991, ApJ, 369, 395

Mezger, P. G., & Henderson, A. P. 1967, ApJ, 147, 471

Minkowski, R. 1946, PASP, 58, 305

Miville-Deschênes, M.A., & Lagache, G. 2005, ApJSS, 157, 302

Nugis, T., & Lamers, H. J. G. L. M. 2000, A&A, 360, 227

Pismis, P., & Recillas-Cruz, E. 1979, Rev. Mex. Astron. Astrofis., 4, 271

Price, S. D., Egan, M. P., Carey, S., Mizuno, D., & Kuchar, T. 2001, AJ, 121, 2819

Raga, A. C., Noriega-Crespo, A., Cantó, J., et al. 1997, RMxAA, 33, 73

Reich, W., Reich, P., & Fürst, E. 1990, AAS, 83, 539

Sharpless, S. 1959, ApJS, 4, 257

Stil, J. M., Taylor, A. R., Dickey, J. M., et al. 2006, AJ, 132, 1158

Van Buren, D., & McCray, R. 1988, ApJ, 329, L93

Van Buren, D., Mac Low, M.-M., Wood, D. O. S., & Churchwell, E. 1990, ApJ, 353, 570

van der Hucht, K. A., Jurriens, T. A., Wesselius, P. R., et al. 1985, A&A, 145, L13

van der Hucht, K. A. 2001, New Astron. Rev., 45, 135

van der Sluys, M. V., & Lamers, H. J. G. L. M. 2003, A&A, 398, 181

Weaver, R., McCray, R., Castor, J. I., Shapiro, P., & Moore, R. 1977, ApJ, 218, 377

Whittet, D. C. B. 2003, Dust in the galactic environment, 2nd Ed. (London: The Institute of Physics)

Wilkin, F. P. 1996, ApJ, 459, L31

Williams, D. R. W. 1973, A&AS, 8, 505

Wilson, R. E. 1953, General Catalogue of Stellar Radial Velocities, Carnegie Inst. Washington D. C. Publ. 601